arXiv:0710.4244v2 [astro-ph] 24 Oct 2007

Near-Field Radio Holography of Large Reflector Antennas

J. W. M. Baars, R. Lucas, J. G. Mangum, and J. A. Lopez-Perez

***Abstract*— We summarise the mathematical foundation of the holographic method of measuring the reflector profile of an antenna or radio telescope. In particular, we treat the case, where the signal source is located at a finite distance from the antenna under test, necessitating the inclusion of the so-called Fresnel field terms in the radiation integrals. We assume a "full phase" system with reference receiver to provide the reference phase. We describe in some detail the hardware and software implementation of the system used for the holographic measurement of the 12m ALMA prototype submillimeter antennas. We include a description of the practicalities of a measurement and surface setting. The results for both the VertexRSI and AEC (Alcatel-EIE-Consortium) prototype ALMA antennas are presented.**

***Index Terms*— ALMA, Antenna measurements, radio holography, millimeter antenna, near-field, radio telescope.**

I. Introduction

LARGE reflector antennas, as those used in radio astronomy and deep-space communication, generally are composed of a set of surface panels, supported on three or more points by a support structure, often called the backup structure. After assembly of the reflector it is necessary to accurately locate the panels onto the prescribed paraboloidal surface in order to obtain the maximum antenna gain. The fact that some antennas have a "shaped"contour is irrelevant for the purpose of our discussion. We are concerned with describing a method which allows us to derive the position of the individual panels in space and compute the necessary adjustments of their support points to obtain a continuous surface of a certain prescribed shape.

The analysis by Ruze [1] of the influence of random errors in the reflector contour on the antenna gain indicates that the RMS error should be less than about one-sixteenth of the wavelength for acceptable performance. Under the assumption that the errors are small compared to a wavelength, randomly distributed with RMS value ϵ, have a correlation length **c** which is much larger than the wavelength λ, and much smaller than the reflector diameter D, the relative decrease in aperture efficiency (or gain) can be expressed by the simple formula

$$\frac{\eta_A}{\eta_{A0}} = \exp\left\{-\left(\frac{4\pi\epsilon}{\lambda}\right)^2\right\}, \qquad (1)$$

where η_{A0} is the aperture efficiency of the perfect reflector. An error ϵ of λ/40 is required to limit the gain loss to 10 percent; with an error of λ/16 the gain is decreased to about half of the maximum achievable.

The setting of the reflector panels at accuracies better than 100 μm has required the development of measuring methods of hitherto unsurpassed accuracy. It should be noted that these measurements need to be done "in the field", which in the case of millimeter radio telescopes generally means the hostile environment of a high mountain site. One versatile, and by now widely used method is normally called "radio holography". The method makes use of a well-known relationship in antenna theory: the far-field radiation pattern of a reflector antenna is the Fourier Transformation of the field distribution in the aperture plane of the antenna. Note that this relationship applies to the amplitude/phase distributions, not to the power pattern. Thus, if we can measure the radiation pattern, in amplitude and phase, we can derive by Fourier Transformation the amplitude and phase distribution in the antenna aperture plane with an acceptable spatial resolution. Bennett *et al.* [2] presented a sufficiently detailed analysis of this method to draw the attention of radio astronomers. Scott & Ryle [3] used the new Cambridge 5 km array to measure the shape of four of the eight antennas, using a celestial radio point source and the remaining antennas to provide the reference signal. Simulation algorithms were developed by Rahmat-Samii [4] and others, adding to the practicability of the method. Using the giant water vapour maser at 22 GHz in Orion as a source Morris *et al.* [5] achieved a measurement accuracy of 30 μm and were able to set the surface of the IRAM 30-m millimeter telescope to an accuracy of better than 100 μm.

Artificial satellites, radiating a beacon signal at a fixed frequency have also been used as farfield ($R_f = \frac{2D^2}{\lambda}$) signal sources. Extensive use has been made of synchronous communication satellites in the 11 GHz band [6], [7]. These transmitters of course do not provide the range of elevation angles accessible with cosmic sources. Some satellites, notably the LES (Lincoln Experimental Satellite) 8 and 9, have been used for radio holography of millimeter telescopes [8]. They provided a signal at the high frequency of 37 GHz and with their geo-synchronous orbit moved over some 60 degrees in elevation angle. Unfortunately, both satellites are no longer available. Lacking a sufficiently strong source in the farfield, we have to take recourse to using an earth-bound transmitter. In practice these will be located at a distance of several hundreds of meters to a few kilometers and be at an elevation angle of less than 10 degrees. Clearly, these are in the nearfield of the antenna, requiring significant corrections to the received signals. In particular, the phase front of the incoming waves

Manuscript received February 21, 2006; revised November 30, 2006.

The performance results presented in this publication were part of a comprehensive technical evaluation process used to evaluate the ALMA prototype antennas which concluded in April 2005.

1045–9243/00$00.00 © 2007 IEEE

will not be plane and it contains higher order terms in the radial coordinate of the antenna aperture. These must be corrected before the Fourier transformation can be applied. We treat these corrections in detail in this paper.

Successful measurements on short ranges have been reported for the University of Texas millimeter telescope [9], the IRAM 30-m telecope [10], the JCMT [11] and the ASTE antenna of NAOJ [12].

ALMA (Atacama Large Millimeter Array) is a new large aperture synthesis array for submillimeter astronomy consisting of 50 high accuracy antennas of 12 m diameter. The instrument is under construction at 5000 m altitude in the Atacama desert of northern Chile. ALMA is a collaboration of North America and Europe with participation of Japan. Two prototype antennas were procured and erected at the site of the Very Large Array of NRAO in New Mexico. The results of an extensive evaluation program of these antennas has been presented by Mangum *et al.* [13]. The reflector surface accuracy was specified at 20-25 μm, requiring a measurement method with an accuracy of 10 μm or better. This was achieved with a near-field holographic system using a transmitter at a wavelength of 3 mm and at a distance of only 315 m from the antennas at an elevation angle of 9 degrees. Here we describe these measurements in some detail.

II. The Mathematics of Radio Holography

The reciprocity theorem describes the equivalency between the characteristics of a transmitting and receiving antenna. Thus both concepts will be used in the following treatment depending on the specific aspect under description. We shall not repeat here the fundamental analysis which leads from Maxwell's equations to the "physical optics" representation of the characteristics of the reflector antenna (*e.g.* [14], [15]). Our discussion below essentially follows the treatment by Silver [14]. The basic expression, linking the radiation function $f(x,y,z)$ at a point P in space with the field distribution $F(\xi,\eta)$ over the aperture plane of the antenna, is written as (see Fig. 1 for the geometry)

$$f(x,y,z) = \int \frac{F(\xi,\eta)e^{-ikr}}{4\pi r} \left[\left(ik+\frac{1}{r}\right)\boldsymbol{i_z}\cdot\boldsymbol{r_1} + ik\boldsymbol{i_z}\cdot\boldsymbol{s}\right] d\xi d\eta, \qquad (2)$$

where the integration is extended over the aperture area, $k = 2\pi/\lambda$ and the unit vectors are as indicated in Fig. 1 (with **s** the propagation vector of the wave field in the aperture). This relation assumes that the aperture is large in units of the wavelength. This general expression can be simplified depending on the distance of the field point P from the aperture plane. We discern the so-called far-field region (Fraunhofer diffraction), near-field region (Fresnel diffraction) and the evanescent-wave zone up to a few wavelengths from the reflector. In the evanescent-wave zone, which does not concern us here, no approximations are allowed.

If the field point P is sufficiently far away from the aperture, the following simplifications can be introduced in the evaluation of Eq. 2:

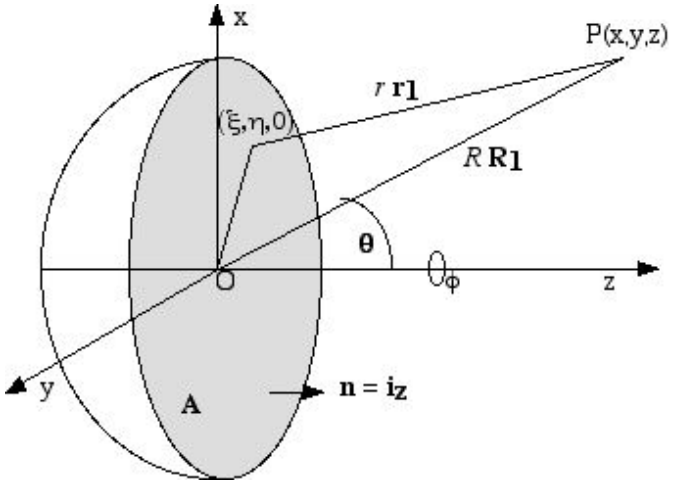

Fig. 1. Geometry of the aperture integration method for finite distance to the field point P.

1) The term $\frac{1}{r}$ is ignored with respect to k in the bracketed term.
2) The term $\frac{1}{r}$ outside the brackets is replaced by the reciprocal distance $\frac{1}{R}$ from the aperture center to the field point P.
3) The term $\boldsymbol{i_z}\cdot\boldsymbol{r_1}$ can be approximated by $\boldsymbol{i_z}\cdot\boldsymbol{R_1} = \cos\theta$ with $\boldsymbol{R_1}$ the unit vector from the origin to the field point.
4) the term $\boldsymbol{i_z}\cdot\boldsymbol{s}$ represents a deviation from uniform phase over the aperture. If these are small, this term can be assumed to be equal to one over the aperture.

With these approximations Eq. 2 is simplified to

$$f(x,y,z) = \frac{i}{2\lambda R}\int F(\xi,\eta)\left[\cos\theta+1\right]e^{ikr}d\xi d\eta. \qquad (3)$$

For the distance r from any point in the aperture to the field point P we have (see Fig. 1)

$$r = \left\{(x-\xi)^2+(y-\eta)^2+z^2\right\}^{0.5}. \qquad (4)$$

Writing the coordinates of the field point P(x,y,z) in spherical coordinates, we obtain

$$\begin{aligned} x &= R\sin\theta\cos\phi \equiv Ru, \\ y &= R\sin\theta\sin\phi \equiv Rv, \\ z &= R\cos\theta = R\sqrt{(1-u^2-v^2)}, \end{aligned} \qquad (5)$$

where we have also introduced the **direction cosines** of the field point

$$P(u,v) = (\sin\theta\cos\phi, \sin\theta\sin\phi).$$

Thus, Eq. 4 can be written as

$$\begin{aligned} r &= \left\{(Ru-\xi)^2+(Rv-\eta)^2+R^2(1-u^2-v^2)\right\}^{0.5} \\ &= R\left\{1-2\frac{u\xi+v\eta}{R}+\frac{\xi^2+\eta^2}{R^2}\right\}^{0.5}. \end{aligned} \qquad (6)$$

The series expansion of Eq. 6 yields

$$r \approx R - (u\xi + v\eta) + \frac{\xi^2+\eta^2}{2R} - \frac{(\xi^2+\eta^2)^2}{8R^3} - \frac{(u\xi+v\eta)^2}{2R} + \frac{(\xi^2+\eta^2)(u\xi+v\eta)}{2R^2} - \dots \quad (7)$$

A. The Far-Field Approximation (Fraunhofer Region)

In the **far-field** situation, where R tends to infinity and $\boldsymbol{R_1}$ and $\boldsymbol{r_1}$ are essentially parallel, the variation of r in the exponent of Eq. 3 can be reduced to the linear part of Eq. 7

$$r = R - (u\xi + v\eta) \quad (8)$$

Additionally, considering that for a high gain antenna the angular region of interest is confined to small values of θ, we can write Eq. 3 with $\cos\theta = 1$, which is valid to 0.1% for angles up to 3 degrees off-axis. The radiation integral (Eq. 3), then becomes

$$f(u,v) = \frac{i}{\lambda}\frac{e^{-ikR}}{R}\int F(\xi,\eta)\exp\{-ik(\xi u+\eta v)\}d\xi d\eta \quad (9)$$

where the integration is performed over the aperture A. We see from Eq. 9 that there exists a Fourier Transformation relationship between $f(u,v)$ and $F(\xi,\eta)$. Ignoring the term $\frac{i}{\lambda}$, the inverse Fourier transformation can thus be written as

$$F(\xi,\eta) = \frac{1}{4\pi}\frac{e^{ikR}}{R}\int f(u,v)\exp\{ik(u\xi+v\eta)\}dudv, \quad (10)$$

where the integration in principle has to be performed over a closed surface, surrounding the aperture. Thus a knowledge of the entire far-field pattern $f(u,v)$ both in amplitude and in phase provides a description of the complex field distribution $F(\xi,\eta)$ over the aperture plane of the antenna, also in amplitude and phase. This forms the basis of the so-called *radio holographic measurement* of the shape of a reflector antenna. Deviations from a uniform phase function over the aperture are thereby linked to local errors in the prescribed contour of the reflector surface.

It is interesting to note that Silver devotes a lengthy discussion to this Fourier Transform relationship ([14], Ch. 6.3), but concludes that the practical application is limited by the fact that the far-field pattern is only prescribed in power. Thus the phase function of $f(u,v)$ would be arbitrary and the aperture distribution cannot be uniquely determined. It was Jennison [16] who mentioned the same relation and its practical usefulness, pointing out that the amplitude and phase can both be measured with an interferometer. When Silver wrote his text in the mid-1940s, radio interferometry had not yet been developed.

In most cases it will be impossible, or in any case impractical, to measure the far-field pattern over the entire sphere. The Nyquist sampling theorem shows however that a measurement of the pattern out to an angle Θ = n Θ_A from the beam axis yields the aperture distribution with a spatial resolution of $\delta = \frac{D}{n}$, where $\Theta_A \approx \frac{\lambda}{D}$ is the half-power beam-width, D is the aperture diameter, and λ the wavelength.

B. The Near-Field Approximation (Fresnel Region)

In the **near-field** region, which corresponds to the Fresnel region in optical diffraction (*e.g.* [17]) most of the simplifications leading to Eq. 3 can still be used, as long as r is at least several aperture diameters large. However, the variation in r over the aperture must now include higher-order terms in Eq. 7 and be maintained in the exponent (phase) term of the integral. Normally, for the Fresnel region analysis, the series is stopped after the quadratic term, which preserves the first three terms of the series in Eq. 7. Thus the near-field (Fresnel region) expression can be written in the form of the following radiation integral, which is the well-known Fresnel diffraction integral in two coordinates:

$$f(u,v) = \frac{i}{\lambda}\frac{e^{ikR}}{R}\int F(\xi,\eta) \exp\left\{ik\left[-(u\xi+v\eta) + \frac{\xi^2+\eta^2}{2R}\right]\right\}d\xi d\eta. \quad (11)$$

In the application of holography in the near-field we want to derive the complex aperture field distribution from the measured near-field pattern. Thus the inverse Fourier Transformation of Eq. 3 will be our point of departure, where Eq. 6 is the expression for the finite distance from a point in the aperture to the point where the signal source is located. Thus we have the inverse of Eq. 3

$$F(\xi,\eta) = \frac{i}{\lambda R}\int f(u,v)\exp(-ikr)dudv. \quad (12)$$

where R is the distance from the antenna aperture center to the holography signal source. We maintain all terms of Eq. 7 in order to make an estimate of the error with respect to the usual Fresnel approximation.

We rewrite Eq. 7 as follows:

$$r \approx R - (u\xi+v\eta) + \delta p_1(\xi,\eta) + \epsilon \quad (13)$$

where we define the terms, which are independent of the integration variables, as the variable δp_1:

$$\delta p_1(\xi,\eta) = \frac{\xi^2+\eta^2}{2R} - \frac{(\xi^2+\eta^2)^2}{8R^3}, \quad (14)$$

while the other terms in higher powers of (u,v) are collected under the variable ϵ.

$$\epsilon = -\frac{(u\xi+v\eta)^2}{2R} + \frac{\left(\xi^2+\eta^2\right)(u\xi+v\eta)}{2R^2}, \quad (15)$$

Substitution of Eq. 7 into Eq. 12 yields

$$F(\xi,\eta) = \frac{i}{\lambda}\frac{e^{-ikR}}{R}\exp\{-ik\delta p_1(\xi,\eta)\} \int f(u,v)\exp\{ik(u\xi+v\eta)\}e^{-ik\epsilon}dudv, \quad (16)$$

The terms in ϵ "modify" the direct Fourier transformation of Eq. 16.

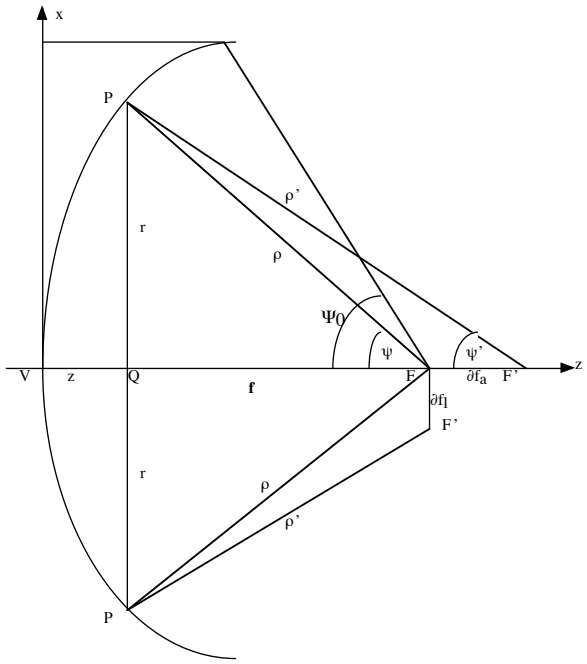

Fig. 2. The geometry of axial (upper half) and lateral (lower half) displacement of the feed from the focus of a parabola.

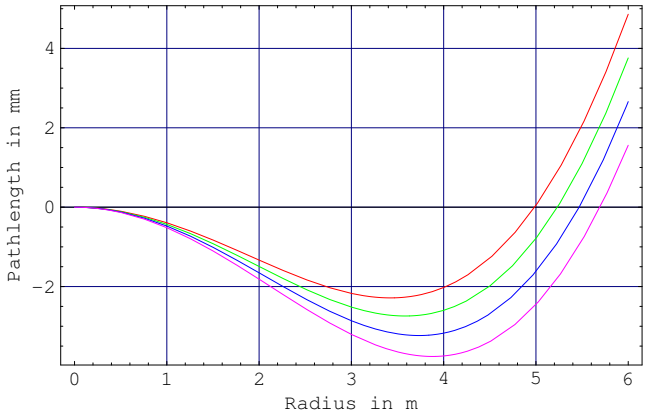

Fig. 3. The residual path-length error ($\delta p_1 + \delta p_2$) in mm for a distance R = 315 m to the holography transmitter and the ALMA 12-m diameter antenna with $\frac{f}{D} = 0.4$. The parameter is the axial defocus δf = 96, step 2, 102 mm, from top to bottom.

1) The δp_1 Term: The first path-length term δp_1 causes a rapidly varying phase variation over the aperture, which can be compensated to a large degree by an axial displacement of the feed. In Fig. 2 we illustrate the geometry of both a lateral δf_l and an axial δf_a displacement of the feed from the primary focus. We need to calculate the difference in path-length $(\rho' - \rho)$ as a function of the radial position r of the point P. The residual path-length error at P with respect to the ray to the vertex V will then be given by

$$\begin{aligned} \delta p_2(\xi,\eta) &= \delta p_2(r) \\ &= (\rho' - \rho)_P - (\rho' - \rho)_V \,, \end{aligned} \tag{17}$$

where $r^2 = \xi^2 + \eta^2$. Applying Pythagoras' law to the upper triangle PQF′ and using the defining relation for the parabola $r^2 = 4fz$, where $z = VQ$, we find for the path-length variation due to an axial defocus δf away from the reflector

$$\begin{aligned} \delta p_2(\xi,\eta) &= \left\{ \xi^2 + \eta^2 + \left(f - \frac{\xi^2+\eta^2}{4f} + \delta f \right)^2 \right\}^{0.5} - \\ &\quad \left\{ f + \frac{\xi^2+\eta^2}{4f} + \delta f \right\}. \end{aligned} \tag{18}$$

We want to minimise the sum of the two terms $(\delta p_1 + \delta p_2)$ (Eqs. 14 and 18) by choosing the appropriate value of δf. Because of the (ξ,η)-dependence there will be a residual path-length error, which we must apply to the result of the Fourier Transformation. Fig. 3 shows the residual path-length error $(\delta p_1 + \delta p_2)$ for several choices of δf for the geometry of the ALMA antennas and the actual distance to the holography transmitter. A value of 96–98 mm limits the error to ± 3 mm over the aperture for R = 315 m. This remaining error must be introduced in the mathematical analysis of the data according to the curve shown in Fig. 3. This is a correction to the aperture phase distribution, obtained after the Fourier Transformation of the measured beam pattern.

2) The ϵ Term: The higher order terms in Eq. 15 (ϵ), containing the integration variables (u, v), constitute a small path-length error which adds a phase term to the integral in Eq. 16 of the form

$$\begin{aligned} \exp(-ik\epsilon) &\approx 1 - ik\epsilon \\ &= 1 - ik \left\{ u\frac{\xi(\xi^2+\eta^2)}{2R^2} + v\frac{\eta(\xi^2+\eta^2)}{2R^2} - \right. \\ &\quad \left. u^2\frac{\xi^2}{2R} - v^2\frac{\eta^2}{2R} - uv\frac{\xi\eta}{R} \right\}. \end{aligned} \tag{19}$$

It is seen that this correction involves the calculation of five additional integrals, which look like Fourier transformations, but aren't really *bona fide* Fourier transformations. When all the integrals of Eq. 19 are evaluated, it turns out that the contribution of ϵ amounts to 2μm of path-length over most of the aperture, reaching a peak value of 10μm at the very edge of the aperture. This is illustrated in Fig. 4. In a high accuracy measurement, where the aim is to achieve a measurement accuracy of better than 10 μm, it is advisable to include this correction term.

3) Dependence on Aperture Plane Reference: In the corrections for the finite distance to the transmitter (the near-field corrections), we define the aperture plane at a convenient location, normally halfway between the vertex and the edge of the reflector. We have taken the center of this aperture plane as the origin of the coordinate system. In most antennas there is a significant distance between this plane and the axes of rotation for the movement of the reflector (see Fig. 5). From this figure we see that there is a "parallax" effect between the adopted direction cosines (u, v) and those given by the antenna scanning coordinates (u′, v′), given by the relations

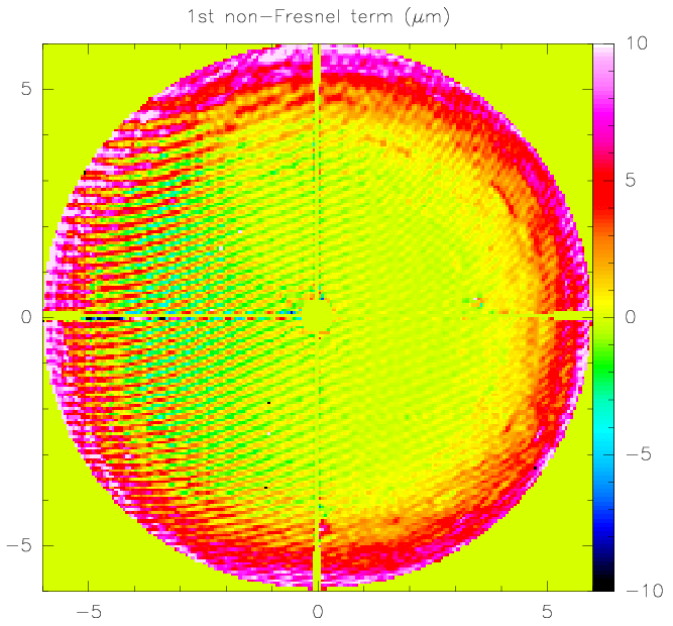

Fig. 4. Non-Fresnel correction terms over the aperture of the 12 m diameter ALMA antenna. Horizontal and vertical axes units are meters with color showing surface error in μm shown at right. The departures from circular symmetry are due to the effects of the actual surface errors present in the map.

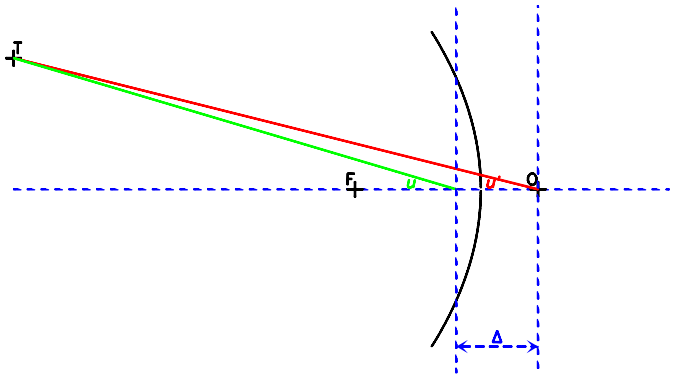

Fig. 5. Illustration of the geometry of selected aperture plane and antenna rotation axis. T is the position of the transmitter while scanning the antenna.

$$\begin{aligned} u &= u'\left(1+\frac{\Delta}{R}\right) \\ v &= v'\left(1+\frac{\Delta}{R}\right), \end{aligned} \tag{20}$$

where Δ is the distance between rotation axis and aperture plane. We use the scanning coordinates (u′, v′), read from the antenna encoders, to calculate the position of the points in the aperture plane. If (u, v) in the Fourier integral (Eq. 16) are approximated by (u', v'), the scale of the aperture map will be overestimated by the factor $\left(1+\frac{\Delta}{R}\right)$. The result of this is that the near-field correction for each pixel in the map is not evaluated at the correct radius. This causes a path-length error proportional to the derivative of the near-field correction with respect to the radial coordinate. Fig. 6 illustrates the magnitude of this effect for the case of our geometry, where $\Delta \approx 3.1$m, *i.e.* about 1% of the distance R to the transmitter. The error is

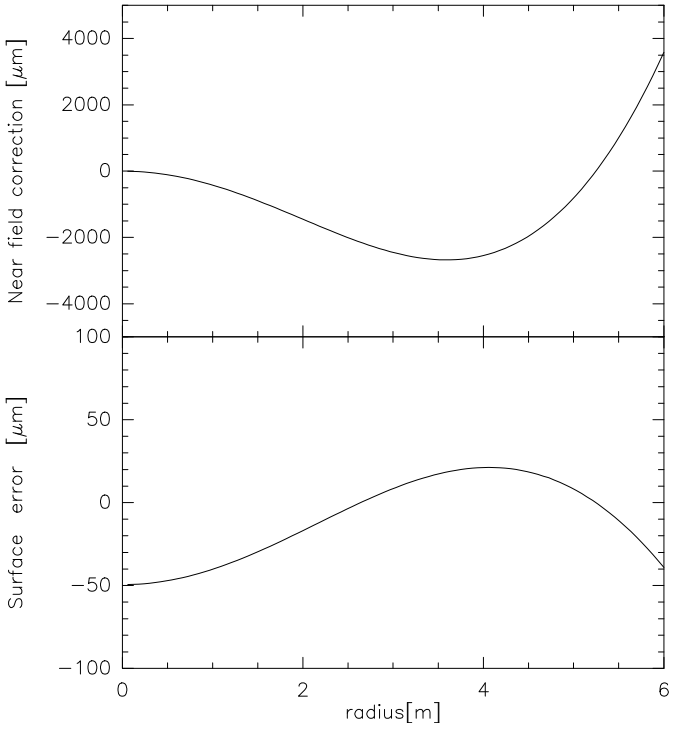

Fig. 6. Top: The near-field path-length correction as a function of radius assuming Δ = 3.1 m and R = 315 m. Bottom: The surface error resulting from the misregistration of the radial coordinate (*i.e.* ignoring the difference between direction cosines u and u').

significant, causing a surface error as a function of radius as shown in the lower part of Fig. 6; its RMS value is 18μm in our case, significant with respect to the required setting accuracy. Such a donut-shaped systematic deviation was indeed found in our original maps, once we applied the geometry correctly. It was of course treated properly in the final measurements and surface setting.

4) Dependence on Focal Deviation: It is possible that during the measurement the receiver feed is not located in the optimum focal position. With reference to Fig. 2 and Eq. 18 it can be shown that the path-length error caused by an axial defocus of δz is given by

$$\delta p_z = \delta z \left\{ 1 - \frac{1 - \frac{\xi^2+\eta^2}{4f^2} + \frac{\delta f}{f}}{\sqrt{\frac{\xi^2+\eta^2}{4f^2} + \left(1 - \frac{\xi^2+\eta^2}{4f^2} + \frac{\delta f}{f}\right)^2}} \right\}, \tag{21}$$

while a transverse (lateral) offset by an amount δx in the ξ-plane (Fig. 2, lower half) will cause a path-length variation of

$$\delta p_x = \delta x \frac{\xi}{f} \left\{ \frac{1}{1+\frac{\delta f}{f}} - \frac{1}{\sqrt{\frac{\xi^2+\eta^2}{f^2} + \left(1 - \frac{\xi^2+\eta^2}{4f^2} + \frac{\delta f}{f}\right)^2}} \right\}. \tag{22}$$

In the reduction process of the holography data, these terms are found by a fit of the measured beam map. The final map of surface deviations is then referred to a position of the feed in the fitted "out-of-focus" location.

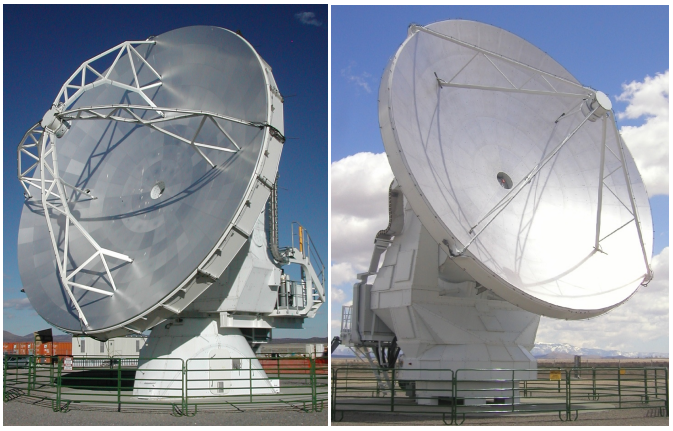

Fig. 7. The VertexRSI (left) and AEC (right) ALMA prototype antennas.

III. Practical Application of the Holography Measurements

A. Task

We now describe the way in which a holography measurement has been executed on the ALMA prototype antennas (Fig. 7). The specification requires the antennas to have a surface accuracy of 25μm RMS for the AEC antenna (with a goal of 20μm) and 20μm for the VertexRSI antenna. ALMA assumed the task to demonstrate this with the aid of a holography system at 3 mm wavelength after delivery of the antennas by the contractors with a surface accuracy of not worse than 100μm RMS. This initial setting was performed by VertexRSI with digital photogrammetry and by AEC with the aid of a Leica "total station" laser-tracker (essentially a theodolite with integrated distance measurement instrument and all-electronic readout).

The holography system was designed to provide a measurement repeatability of 10μm, which would suffice to demonstrate the realism in the obtained overall surface accuracy. It should be noted that in the current setup the holography system provides a surface map at one elevation only. No information on the gravitational deformation of the antenna with varying elevation angle can be obtained.

B. Equipment and Measurement Program

- The signal source for the holography measurements is a monochromatic transmitter at a frequency of 78.92 or 104.02 GHz, located on a 50 m high tower at a distance of 315 and 302 m from the VertexRSI and AEC antenna, respectively. The elevation angle is approximately 9 degrees.
- The receiver is a full-phase double-receiver, located in the apex region behind the primary focus of the main antenna. The reference signal is received by a wide beam horn pointing along the boresight towards the transmitter.
- Amplitude and phase maps of the antenna beam were obtained by raster scanning. The Nyquist sampling theorem provides the link between the angular size of the observed map and the required spatial resolution over the aperture. If we want to obtain n independent samples over the diameter of the aperture, we need to extend the map to an angle of n times the half-power beamwidth off axis. We chose a map size to obtain about 0.15 m spatial resolution after Fourier transformation of the map. A typical measurement then takes about one hour of time.
- From the phase distribution, which is a representation of the misalignment of the 264 (VertexRSI) or 120 (AEC) panels constituting the reflector, the necessary adjustments of the 5 support points per panel were derived. These were then applied by hand with a simple tool to improve the accuracy of the reflector surface.

The algorithms and software used for the data analysis and derivation of the panel adjustments have been applied successfully at the telescopes of IRAM. The necessary corrections for the finite distance to the transmitter (the "near-field" corrections) in our case were derived and checked against similar corrections applied by others, *e.g.* for the JCMT [11].

The equipment has been designed to provide sufficient signal–to–noise ratio to render the error due to noise insignificant. The greatest risk in this type of measurement lies in undetected or poorly corrected *systematic errors*.

- An accurate knowledge of the amplitude and phase function of the feedhorn, illuminating the reflector, is essential, because errors in these are fully transferred to the aperture phase map and hence to the surface profile.
- Multiple reflections from the ground or structures form a possible source of errors in this type of work. We carefully covered all areas of potentially harmful reflections with absorbing material. In some controlled experiments we could not demonstrate the existence of reflections.
- The dynamic range of the receiver must be sufficient to accommodate the strong signal on the peak of the beam and the very weak signals towards the edge of the scan. There might have been some saturation on some of the measurements. We discuss this in more detail below.
- The effect of the finite distance of the transmitter can be removed to a large extent (but not completely) by an axial shift in the position of the feed. An error in the distance to the transmitter thus can be corrected in the data analysis by a small adjustment of the feed position. The remaining phase error can be accurately calculated and applied to the data.

C. Holography System Hardware

The hardware specifications and requirements are summarised in Tables I and II. In the following we briefly describe the hardware components that comprise the holographic measurement system.

1) Front-End: The front-end (see Fig. 8) is enclosed in a small, temperature controlled box with a diameter of about 30 cm and a length of 50 cm. It fits inside the "apex structure" behind the primary focus of the VertexRSI antenna. The AEC antenna does not provide such a wide space and the receiver is bolted to the outside flange of the apex structure with a long piece of waveguide bringing the signal feed in focus. Both the signal– and reference–receiver are housed "back-to-back" in this box. This provides a compact system in which the LO

TABLE II
HOLOGRAPHY HARDWARE SPECIFICATIONS

Frequencies	78.92 and 104.02 GHz
Frequency Stability	$\leq \pm 5$ Hz/day
Receiver Bandwidth	10 kHz
Receiver Tunability	130 MHz
Transmitter Antenna Gain	33dB
Transmitter EIRP (P)	$> 20\mu$W
Transmitter Power to Antenna	> 10nW
Transmitter Antenna Beam-Width @ -3dB	4.6 deg (twice antenna angle at xmtr)
Reference Antenna Beam-Width @ -3dB	4.6 deg (twice scan range)
Main Feed Beam-Width @ -3dB	128 deg (-3dB edge taper)
System Temperature	3200 K
Reference Feed Power Received (P_r)	$1.7 \times 10^{-9} P$
On-Boresight Signal (M_0)	$4.2 \times 10^{-7} P$
On-Boresight Noise (σ_0)	$\left(1.2 \times 10^{-22} W(P)\right)^{\frac{1}{2}}$
Off-Boresight Noise (P_r Term)	$\left(2.1 \times 10^{-27} W(P)\right)^{\frac{1}{2}}$
Average map noise for complex correlator (σ_{av})	$\left(2.2 \times 10^{-25} W(P)\right)^{\frac{1}{2}}$

TABLE I
HOLOGRAPHY HARDWARE REQUIREMENTS

Measurement Error	$< 10\mu$m
Phase Accuracy	< 0.3 deg ($2.5\mu m$ @ 3mm) RMS
Amplitude Accuracy	$< 1\%$
Dynamic Range	$\geq$ 43dB
Signal-to-Noise Ratio (SNR)	$\geq$ 40dB
Channel-to-Channel Isolation	$>$ 100dB
Data Rate	$\sim$ 80 samples/sec (12 msec)

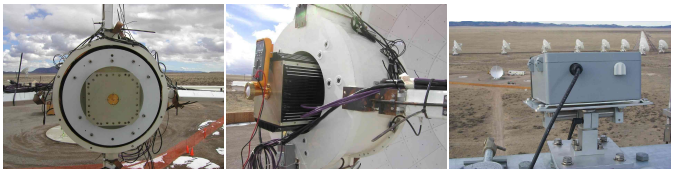

Fig. 8. Holography system hardware. Left: Signal feed side of the front-end. Middle: Reference feed side of the front-end. Right: transmitter on top of the tower pointing at the VertexRSI prototype antenna in the foreground. The other antennas are part of the NRAO Very Large Array (VLA).

signals can easily be made equal in length, greatly contributing to the phase stability of the system. Broadband mixers at ambient temperature convert the received signal frequency to a baseband of 10 kHz width. The system is designed with two frequencies at 78.9 and 104.02 GHz. Making the measurement at two different frequencies can be helpful in discerning systematic effects in the resulting maps, for instance caused by multiple reflections. The receiver is also tunable around each of these frequencies by 130 MHz for similar reasons. The signal horn is a conical, grooved cylindrical waveguide horn, while the reference horn is of similar design and equipped with a lens to provide a reference beam with a beam-width of 4.6 degrees at the half-power points.

As is clear from the theoretical treatment above, it is imperative that we know the amplitude and phase function of both the reference and the signal feed as accurately as possible. The phase function must be subtracted from the measured aperture phase before connecting its phase variations to errors in the reflector profile. The feedhorns have been measured with great care on the indoor range at IRAM in Grenoble [18]. The results were compared with model calculations using an advanced electro-magnetic simulation package (the FDTD package of Microwave Studio from Computer Simulation Technology) and excellent agreement was found. The phase pattern of the feeds have an estimated error of less than one degree, while the amplitude taper at the edge of the reflector aperture is -6 dB. This is more than we would like (a free–space taper of 2.5 dB has to be added to the measured level). For a high signal to noise ratio in the outer part of the reflector an actual level of -6 dB is preferred. For the measurement of the ALMA production antennas this feed should be replaced by one which provides such a taper.

2) Back-End and Transmitter: The back-end of the receiver is essentially a digital signal processor (DSP) where the narrow-band signals are digitized and correlated. Both the "sine" and "cosine" part of the complex correlation function are obtained, which are then transformed to the amplitude and phase functions.

The transmitter consists of a single photo-diode, directly coupled to a waveguide horn, which is fed through an optical fiber by two optical signals at different frequencies near a wavelength of ~ 1550 nm. The photo-diode provides a mixing signal at the difference of the two optical signals, tunable roughly from 78.7 to 79.0 GHz (low band) and 103.8 to 104.2 GHz (high band), with an output power of about 10 nW, leading to an EIRP of about 20 μW. The transmitter is placed on top of a 50 m high tower at a distance of 300 to 325 m from the aperture of three antennas at the site, resulting in a measurement elevation angle of about 9 degrees.

IV. HOLOGRAPHIC DATA ACQUISITION

To derive typical values for the various holography map parameters, we set the following boundary conditions:

- The data rate is the canonical 12 msec per sample, which means about 80 samples per second.
- The fine tuning feature of the holography receiver allows for the search for ground reflection.
- A goal for the total time for one map is less than one hour.
- The required aperature plane resolution is $\leq$ 20 cm. This yields $\geq$ 25 independent points per square meter of reflector surface.

- The 5 panel support points are on average some 0.4 to 0.6 m apart for the VertexRSI and AEC panels, respectively. A twist in the panel with a similar scale length can be partially corrected. With a measurement spatial resolution of 15–20 cm this large scale twist can be fitted sufficiently well.
- Oversample by a factor of at least 2 to minimize aliasing.

Based on the equations listed in Appendix I, with $f_1 = 1.13(6 + 2.5$ dB taper$)$, we obtain the typical holography map parameters of Table III.

V. Holographic Data Analysis

A. Description

Data analysis uses the CLIC data reduction software of the Plateau de Bure interferometer. The raw data, written by the on-line software in the ALMATI-FITS data format [19], is converted to Plateau de Bure format using CLIC. The data are then calibrated and imaged using CLIC. The two main operations are:

1) *Calibrate data in amplitude and phase*, based on boresight measurements at beginning and end of each map row, assuming gradual drift in amplitude and phase with time. This uses the standard amplitude and phase calibration commands in CLIC, which:
   a) Fit cubic spline functions of time to the observed amplitude and phase data on the boresight measurements.
   b) Subtract the phase spline function from the observed phase for the mapping scans.
   c) Divide the observed amplitude for the mapping scans by the amplitude spline function.
2) *Compute the aperture map and fit panel displacements and deformations*. The data processing steps for computation of the aperture maps are:
   a) *Interpolate data to a regular grid* in the antenna-based coordinate system. This grid matches the observed system of rows (same number and separation). This grid is further extended, by addition of zeroes, to a user-specified size, in order to get a finer interpolation of the output aperture map: 64x64, 128x128, 256x256 and 512x512 sizes are available.
   b) *FFT to aperture plane*. This is replaced by a more complex transformation if one takes into account the first non-Fresnel terms, as described in § II-B (Eq. 16).
   c) *Compute phases in the aperture plane*.
   d) *Apply the geometrical phase correction*: This is Eq. 14 plus Eq. 18, substituting $\rho = \sqrt{\xi 2 + \eta 2}$ as the radius in the aperture, f the focal length of the primary, and δf by the distance between the holographic horn phase center and the antenna prime focus (see §II-B).
   e) *Correct for measured feed phase diagram*. The measurement is described in the memo by Lazareff *et al.* [18].
   f) *Mask edges and blockage*.
   g) *Fit and remove 6 phase terms:* Constant, 2 linear gradients in the horizontal and vertical directions, 3 focus translations. These terms account for a phase offset, an antenna pointing error (constant during the measurement) and a small vector displacement of the holography horn relative to the nominal focus position ($f + \delta f$). The phase terms for the axial and transverse displacements of the focus are given in Eqs 21 and 22 respectively. Optionally one may keep fixed either the δx and δy coordinates or all three δx, δy, and δz coordinates.
3) *Convert to normal displacement map.* See Appendix II for details.
4) *Plot amplitude and phase maps.*
5) *Fit panel displacements (optionally deformations) and screw adjustments*.
   a) Each panel is assumed to be displaced (in the axial direction), tilted (around two orthogonal axes), and possibly deformed (deformation is a quadratic function of position offset relative to the panel center). As there are only five screws, only two deformation modes are allowed, we have thus five displacement modes:

$$\delta p_1(x,y) = a \quad (23)$$
$$\delta p_2(x,y) = bx \quad (24)$$
$$\delta p_3(x,y) = cy \quad (25)$$
$$\delta p_4(x,y) = d(x^2+y^2) \quad (26)$$
$$\delta p_5(x,y) = e(x^2-y^2) \quad (27)$$

   where x and y are coordinates of a point on a panel (x and y in the plane tangent to the panel surface, with x axis in the radial direction).
   b) The five coefficients a, b, c, d, e are independently fitted for each panel to the relevant part of the map for this panel.
   c) To take into account the effects of finite angular resolution, an iterative procedure is used where:
      i) The radiated beam is calculated using the fitted panel surfaces.
      ii) This beam is truncated to the size of the observed beam map, and subtracted from the observed beam.
      iii) An incremental surface map is calculated.
      iv) A new set of incremental panel displacements is calculated from this map.

   The procedure converges after a few iterations. The screw settings are output to a text file.
6) *These screw settings are applied to the panel adjusters* to improve the surface accuracy of the reflector. The adjustments were done with a simple tool. Two people on a manlift approached the surface from the front, where the adjustment screws are located (see Fig. 9). The time needed for an adjustment of the total of 1320/600 adjusters was 8/7 hours for the VertexRSI/AEC prototype antennas, respectively. The entire procedure is

TABLE III
TYPICAL HOLOGRAPHY MAP PARAMETERS

Map Type	δ_d (cm)	f_{osr}	θ_{ext} (deg)	θ_{sr} (arcsec)	$\dot{\theta}$ (arcsec/s)	N_{row}	f_{oss}	t_{map} (hr)
Standard	20	2.2	1.64/1.24	33/25	300	180	20/15	0.96/0.73
Fine	13	2.2	2.46/1.87	33/25	600	270	40/30	1.08/0.82
Course	20	1.4	1.64/1.24	53/40	300	112	20/15	0.61/0.46

Assumes f_1 = 1.13 (6 + 2.5 dB taper), ν = 78.92/104.02 GHz, θ_b = 74/56 arcsec, and $f_{apo} = 1.3$.

Fig. 9. Panel adjustment of the VertexRSI prototype antenna.

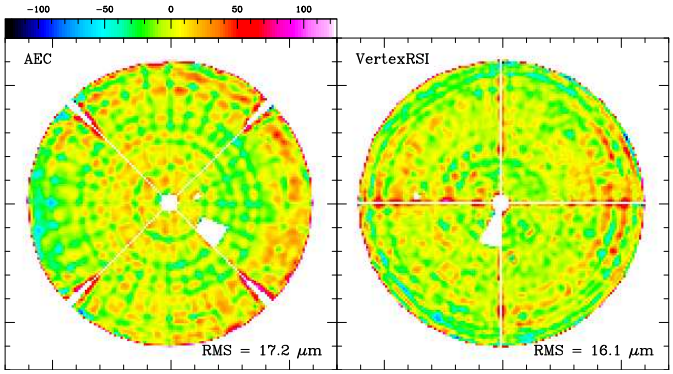

Fig. 10. Final holography maps for the AEC (left) and VertexRSI (right) ALMA prototype antennas. Horizontal and vertical axes units are meters with color scale plotted as surface displacement in μm (top right). Note that the "×" (AEC) and "+" (VertexRSI) feed leg structure and the difficulties encountered with holographic measurements near these structures leads to the poor measurement results in these areas.

repeated until the required accuracy is achieved, or alternatively until the inherent measuement accuracy has been reached and no further improvement is surface accuracy is obtained.

VI. ALMA PROTOTYPE ANTENNA HOLOGRAPHY MEASUREMENT RESULTS

The holographic measurement and setting of both antennas was performed immediately after the antennas became available for evaluation. During a period of about one year the antennas were subjected to a number of hard loads, like fast switching tests, drive system errors resulting in strong vibrations, and high-speed emergency stops collisions. Also, the influence of wind and diurnal temperature variations on the surface stability was a point of concern. It was therefore decided to close the evaluation program with a second holographic measurement of the reflector surfaces. This was done in December 2004 to February 2005 during relatively good atmospheric conditions. It was during these measurements that we discovered that we had not correctly taken care of the correction explained above in §II-B.3. This correction was subsequently applied properly and the final surface maps are shown in Fig. 10. Both antennas were set to a surface accuracy of 16–17 μm RMS.

A. VertexRSI Antenna

1) Overview: The antenna was delivered with a nominal surface error of 80 μm RMS, as determined from a photogrammetric measurement. Our first holography map showed an RMS of approximately 85 μm. A first setting of the surface resulted in an RMS of 64 μm. In four more steps of holographic measurement followed by adjustment the surface error decreased to 19 μm RMS.

The sequence of surface error maps, along with the RMS and the error distribution is shown in Fig. 11. As allowed in the specification, we have applied a weighting over the aperture proportional to the illumination pattern of the feed. This essentially diminishes the influence of the surface errors in the outer areas of the reflector. The white areas in the surface error maps are the quadripod, optical pointing telescope, and a few bad panels, which could not be set accurately. All of these structures were left out of the calculation of the final overall RMS value.

With increasing accuracy the presence of an artefact in the outer area of the aperture became apparent. There is a "wavy" structure in the outer section with a "period" too large to be inherent in the panels. Experiments with absorbing material showed that it was not caused by multiple reflections. The effect can be described by a DC-offset in the central point of the measured antenna map, *i.e.* some saturation on the point with the highest intensity. By adjusting this offset in the software, most of the artefact could be removed. This has been done with the final data. The additional set of follow-up holography measurements in December 2004 – February 2005 did not suffer from this signal saturation, and no artefact was observed in these follow-up maps. Checks of the holography hardware indeed suggest that the 2003 holography measurements did experience a small amount of signal saturation.

The best surface maps were obtained at night. During the spring 2003 period they consistently show an RMS of about 20μm. Daytime maps tend to be somewhat worse; typical values of the RMS lie between 20 and 25μm. Part of this is certainly due to the atmosphere, even over the short path-length of 315 m.

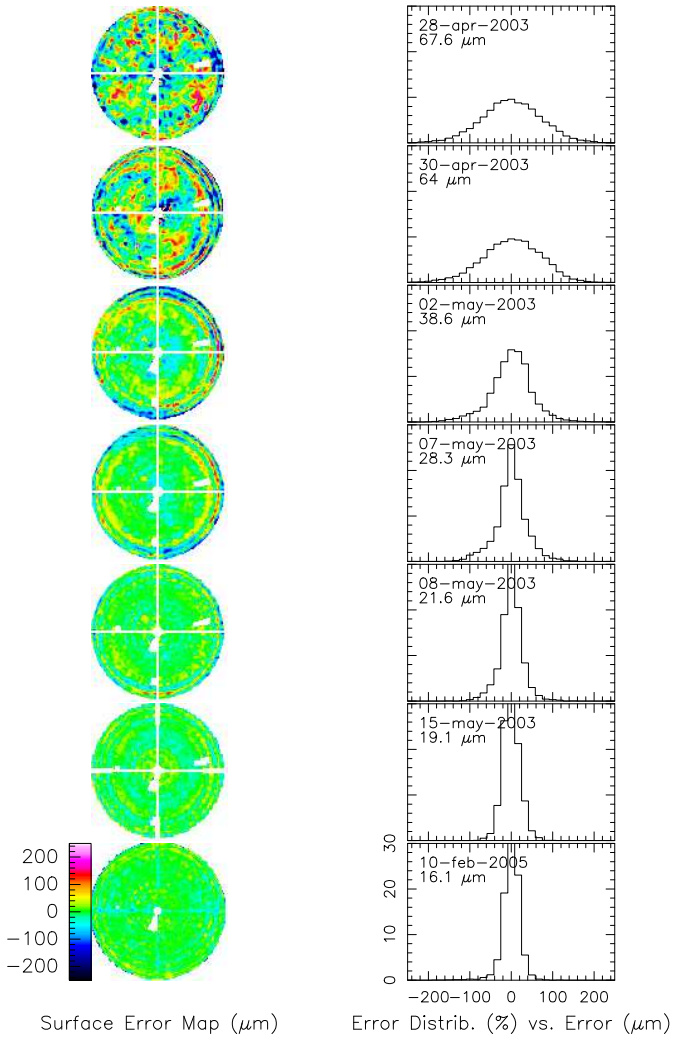

Fig. 11. Sequence of surface error maps with intermediate panel setting. The surface contours are shown on the left side; the error distribution, plotted as percentage contribution versus surface error, on the right. The white cross and the small white areas represent the quadripod and a few faulty panels and were not considered in the calculation of the RMS error. Progression to the final surface RMS included holography system checkout, so does not represent the time required to set the VertexRSI antenna to its final surface.

2) General Surface Stability: To estimate the accuracy and repeatability of the measurements, we produced difference maps between successive measurements throughout the measurement period. The RMS difference between consecutive maps is normally less than 10μm, typically 8μm. An example of a difference map is shown in Fig. 12. The map of measurement number 307 is shown on the left, while the right hand side shows the difference between map 307 and 308, made about one hour later.

We have made many maps after the final setting of the surface while changing the orientation of the antenna with respect to the Sun. Maps taken over a few consecutive days were obtained at widely different temperatures, while also the wind conditions varied over time. The measured rms error during a 30 hour period in early May 2003 varied between 20 and 23μm. During this period the wind was calm ($<$ 5 m/s) and temperature changes of 15 C were encountered. A later

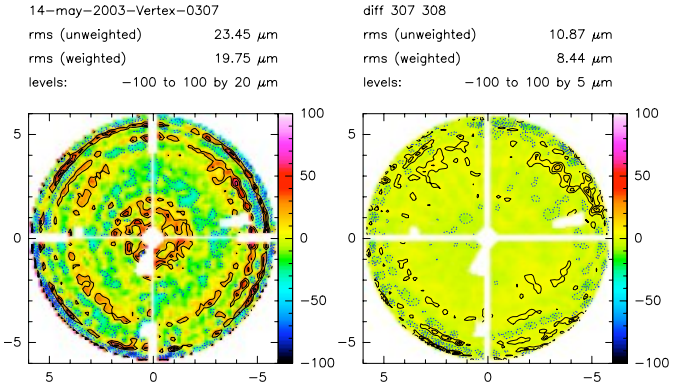

Fig. 12. Example of the repeatability of the measurements. Horizontal and vertical axes units are meters with color scaling showing surface error in μm. The map on the right is the difference between the one at left and a map made one hour afterwards. The RMS of the difference maps is about 8μm, which is commensurate with the expected value due to noise and atmospheric fluctuations.

5 day series in mid June gave rms errors from 22-26μm with temperature variation up to 20 C, wind velocities up to 10 m/s and periods of full sunshine. Most of this increase is believed to be due to the deteriorating atmospheric conditions at the VLA site during summer, when the humidity is significantly higher than normal. The much better results of 17μm obtained during the cold and dry winter period also point to a significant atmospheric component in the spring and summer results.

However, some of the changes will be caused by temperature and wind. To increase the rms from 20 to 22μm, the "additional" component has a magnitude of 9μm rms. Such a contribution can be expected from the calculated values of 4μm each for wind and temperature for the panels, and 5μm for wind and 7μm for temperature for the BUS. These numbers are all within the specification. Actually, the measured differences are close to those expected from the estimated accuracy of the holography measurement and the measured rms differences in consecutive maps of about 8μm.

B. AEC Antenna

1) Overview: The apex structure of the AEC antenna does not enable us to mount the holography receiver inside the cylinder, as in the case of the VertexRSI antenna. Thus in this case the receiver was bolted to the flange on the "outside" of the apex-structure. Consequently, the feedhorn was brought to the required position by a piece of waveguide of about 500 mm length. This caused significant attenuation in the received signal from the reflector to the mixer. Considering the available transmitter power, we concluded that this would not jeopardise our measurement accuracy significantly.

The AEC antenna surface was set by the contractor with the aid of a Leica laser-tracker. The RMS of the surface was reported by the contractor to be 38μm. After this measurement a servo error caused the elevation structure to run onto the hard stops at high speed. The contractor decided to repeat the surface measurement and obtained an RMS of 60μm with some visible "astigmatism" in the surface.

Our first holography map indicated an RMS of 55μm with a clearly visible astigmatism. We could identify the high and

low regions with those on the final AEC measurement. With two complete adjustments we surpassed the goal of 20μm. A third partial adjustment improved the surface RMS to about 14μm. There is no indication of the "artefact" seen in the VertexRSI antenna. The results of the consecutive adjustments are summarised in Fig. 13. The last panel in this figure shows the final map after the repeated measurement and setting in January 2005.

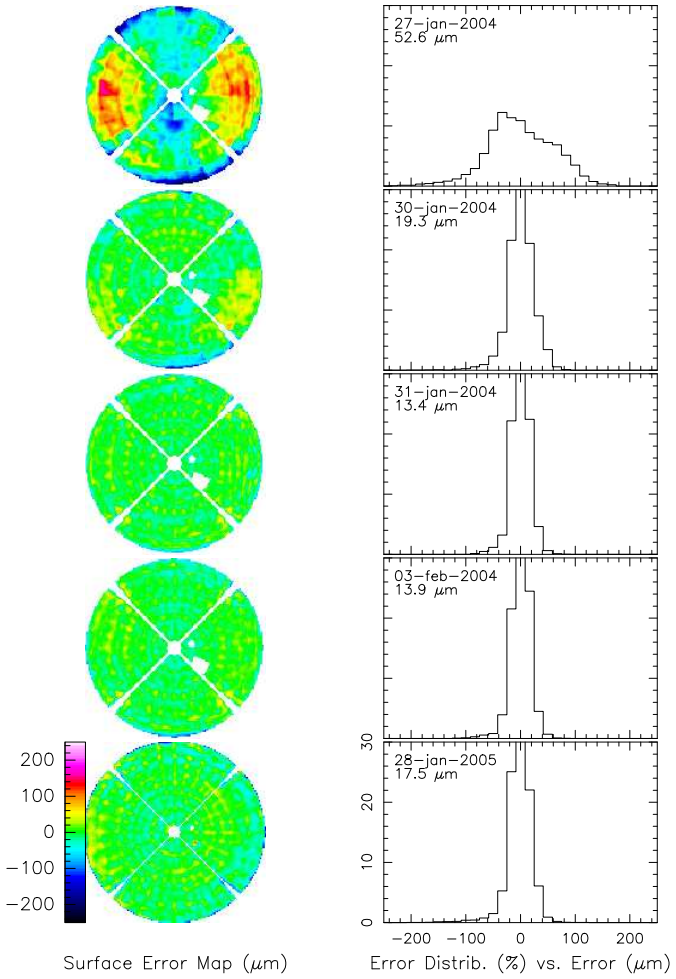

Fig. 13. Sequence of surface error maps with intermediate panel setting. The surface contours are shown on the left side; the error distribution on the right. The white cross and the small white area represent the quadripod and a faulty panel and were not considered in the calculation of the RMS error. Note that the differences between the final three maps is within the overall uncertainty of the holography measurements.

The adjustments were done with a tool provided by the contractor. It was similar to the one used by us on the VertexRSI antenna, but it was calibrated in "turns" rather than in micrometres.

2) General Surface Stability: In Fig. 14 we show one of the final results and a difference map of this and the following measurement, made one hour later. The difference map indicates a repeatability of $\sim 5\mu$m RMS. There is no indication of the "ringing" in the outer region of the aperture, as was the case for the VertexRSI antenna. We ascribe this to the lower signal level due to the long piece of waveguide between feed and mixer.

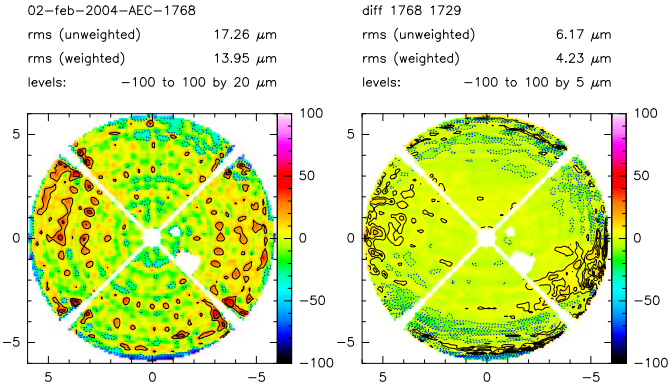

Fig. 14. Example of the repeatability of the measurements. The map on the right is the difference between the one at left and a map made one hour afterwards. The RMS of the difference maps is about 5μm.

Also here we made a series of 16 maps over a period of more than two days in early February 2004. Temperatures ranged from $+2$ to -10 C, while the wind was mostly calm with some periods of speeds up to 10 m/s. During one day there was full sunshine. The measured RMS error is very constant with a peak to peak variation of less than 2μm on an average of 14μm. The differences are fully consistent with the allowed errors under environmental changes and also of the same order as the measurement accuracy. We believe that the significantly better overall result is mainly due to the much drier and stabler atmosphere during these measurements as compared with the summer data from the VertexRSI antenna.

VII. Conclusions

We have successfully performed a holographic measurement and consecutive panel setting of the reflectors of the two ALMA prototype antennas to an accuracy of better than 20 μm. Our estimated measurement accuracy is approximately 5 μm. The data collection and analysis software packages are easy to use and provide quick results of the measurements, directly usable for a panel adjustment setting. We consider this system suitable for the routine setting of the ALMA production antennas to the goal of 20 μm accuracy in an acceptable time span. Modern survey equipment enables contractors to deliver reflectors with an accuracy of 50-60 μm without undue cost. Although the holography system can easily start with a much larger error, in the former case it is feasible to reach the specification with only one panel setting based on holography. We note that these measurements, being performed at one elevation angle only, do not provide information on the gravitationally induced deformation as function of elevation angle.

In summary:

1) The holography system has functioned according to specification and has enabled us to measure the surface of the antenna reflector with a repeatability of better than 10μm.
2) As shown in Figs. 11 and 13, we have set both antenna surfaces to and accuracy of 16-17 μm RMS. This will provide an aperture efficiency of about 65 percent of that of a perfect reflector at the highest observing frequency of 950 GHz.

3) The small differences in the surface maps obtained over several days of measurement are consistent with the measurement repeatability and at best marginally significant. If taken at face value, they indicate that the deformations of the reflector under varying wind and temperature influence are fully consistent with, and probably well within, the specification. This excellent behaviour over time is more important than the actual achieved surface setting. We stopped iteration of the settings after having achieved the goal of less than 20 μm.
4) Further information on the performance of the ALMA Prototype Antennas can be found in [13].

APPENDIX I
HOLOGRAPHY MAP PARAMETER EQUATIONS AND CALCULATIONS

In this appendix we list the equations used to derive the holography measurement values listed in Table III. The calculation leading to the power-related expressions of this appendix are detailed in [20].

$$f_1 \equiv \text{taper factor for signal feed}$$
$$= 1.13(6 + 2.5 \text{ dB taper}) \quad (28)$$
$$f_{apo} \equiv \text{apodization smoothing factor} \quad (29)$$
$$f_{osr} \equiv \text{map oversampling factor between rows} \quad (30)$$
$$f_{oss} \equiv \text{map oversampling factor along a row} \quad (31)$$
$$D \equiv \text{main antenna diameter} \quad (32)$$
$$d \equiv \text{reference feed diameter} \quad (33)$$
$$\theta_{ext} \equiv \text{angular extent of map (assumed square)} \quad (34)$$
$$\theta_b \equiv \text{primary beam size}$$
$$= \frac{f_1 c}{\nu D}$$
$$= \frac{61836.6 f_1}{\nu(GHz) D(m)} \text{ arcsec} \quad (35)$$
$$\theta_{sr} \equiv \text{sampling interval between rows}$$
$$= \frac{\theta_b}{f_{osr}}$$
$$= \frac{f_1 c}{f_{osr} \nu D}$$
$$= \frac{61836.6 f_1}{f_{osr} \nu(GHz) D(m)} \text{ arcsec} \quad (36)$$
$$\theta_{ss} \equiv \text{sampling interval along a scan}$$
$$= \frac{\theta_b}{f_{oss}}$$
$$= \dot{\theta} t_{samp}$$
$$= 0.012 \dot{\theta} \text{ arcsec} \quad (37)$$

$$N_{row} \equiv \text{number of rows in map} \quad (38)$$
$$\delta_d \equiv \text{spatial resolution on dish}$$
$$= \frac{D}{N_{row}}$$
$$= \frac{f_1 f_{apo} c}{\nu \theta_{ext}}$$
$$= \frac{1717.7 f_1 f_{apo}}{\nu(GHz)\theta_{ext}(deg)} \text{ cm} \quad (39)$$
$$\dot{\theta} \equiv \text{map row scanning rate} \quad (40)$$
$$L_m \equiv \text{linear size of map} \quad (41)$$
$$P \equiv \text{Transmitter EIRP} \quad (42)$$
$$P_r \equiv \text{Reference feed power received}$$
$$= \frac{\pi d^2}{4} \frac{P}{4\pi R^2}$$
$$= \frac{1}{16} \left(\frac{d}{R}\right)^2 P \quad (43)$$
$$P_s \equiv \text{Main antenna power received on boresight}$$
$$= \frac{\pi D^2}{4} \frac{P}{4\pi R^2}$$
$$= \frac{1}{16} \left(\frac{D}{R}\right)^2 P \quad (44)$$
$$P_s(\alpha) = P_s(0) \left[\frac{J_1\left(\frac{\pi \alpha D}{\lambda}\right)}{\left(\frac{\pi \alpha D}{2\lambda}\right)}\right]^2 \quad (45)$$
$$\sigma^2 = \frac{\left[k T_{sys} B + P_r + P_s(\alpha)\right] k T_{sys}}{t_{int}} \quad (46)$$
$$\delta z = \frac{\lambda}{16\sqrt{2}} \frac{\sqrt{N_{sx} N_{sy}}}{f_{os}^2} \frac{\sigma_{av}}{M_0}$$
$$= 0.044\lambda \frac{\sqrt{N_{sx} N_{sy}}}{f_{os}^2} \frac{\sigma_{av}}{M_0} \quad (47)$$
$$B \equiv \text{Detector bandwidth} \quad (48)$$
$$t_{int} \equiv \text{Integration time}$$
$$= N_{row} t_{row}$$
$$= \frac{f_{osr} \theta_{ext}^2}{\dot{\theta} \theta_b}$$
$$= \frac{1717.7 \times 10^2 f_{osr} f_1 D(m)}{\dot{\theta}(arcsec/sec)\nu(GHz)\delta_d^2(cm)} \text{ hours} \quad (49)$$
$$\alpha \equiv \text{Scan angle, which ranges over} \pm \frac{\theta_{ext}}{2} \quad (50)$$
$$R \equiv \text{Distance between holography Tx and Rx} \quad (51)$$
$$\Delta z \equiv \text{Reflector surface displacement accuracy} \quad (52)$$

For the ALMA holography system:

1) t_{int} = 36 msec,
2) $M_0 = \sqrt{P_s(0) P_r} = 4.167 \times 10^{-7}$P,
3) $\sigma_0 = \left(1.23 \times 10^{-22} W(P)\right)^{\frac{1}{2}}$,
4) P_r Term = $\left(2.13 \times 10^{-27} W(P)\right)^{\frac{1}{2}}$
5) Average map noise for complex correlator (σ_{av}) = $\left(2.23 \times 10^{-25} W(P)\right)^{\frac{1}{2}}$,
6) $\delta z = \frac{1.35 \times 10^{-2}}{\sqrt{P}}$

Thus, if we want an error in the measurement of the surface shape of δz = 5 μm, we need a transmitter with an EIRP of P = 7.3 μW. The expected radiated power is in excess of 10μW, so there is a good margin. Noise will not be the limiting factor in the accuracy of the measurement.

APPENDIX II
SURFACE RMS CALCULATION DETAILS

The RMS in the holography plots is computed in the following way:

- *Unweighted*:

$$\sigma_u = \sqrt{\frac{1}{N}\sum_i d_i^2 - \left(\frac{1}{N}\sum_i d_i\right)^2} \tag{53}$$

  - The summation is on the N unmasked pixels
  - d_i is the normal surface displacement for pixel i

- *Weighted*:

$$\sigma_w = \sqrt{\frac{1}{\sum_i w_i}\sum_i w_i e_i^2 - \left(\frac{1}{\sum_i w_i}\sum_i w_i e_i\right)^2} \tag{54}$$

  - The summation is on the unmasked pixels
  - e_i is half of the path-length error due to the surface displacement for pixel i. This is directly related to the observed phase errors $\delta\phi_i$ by:

$$\begin{aligned} e_i &= \delta\phi_i \frac{\lambda}{4\pi} \\ &= d_i \cos\alpha_i \end{aligned} \tag{55}$$

  - w_i is the illumination amplitude of an ideal ALMA receiver at pixel i. This is currently specified to a 12dB taper (w_i is 0.251 at the edge of the dish). The function used is parabolic:

$$w_i = 1 - \left(1 - 10^{-0.6}\right)\left(\frac{r_i}{6}\right)^2 \tag{56}$$

  - $\cos(\alpha)$ is a projection factor which attenuates the effect on antenna efficiency of surface errors for rays close to the edge of the dish. This projection factor is:

$$\cos\alpha_i = \frac{1}{\sqrt{1. + \frac{r_i^2}{4f^2}}} \tag{57}$$

ACKNOWLEDGEMENTS

We gratefully acknowledge the support by the staff of NRAO. In particular, we thank Nicholas Emerson, Fritz Stauffer, Jack Meadows and Angel Otárola for their work on the soft- and hardware and panel adjustments.

REFERENCES

[1] J. Ruze, "Antenna Tolerance Theory - A Review", *Proc. IEEE*, **54**, 1966, pp. 633-640.

[2] J. C. Bennett, A. P. Anderson, P. A. McInnes and A. J. T. Whittaker, "Microwave holographic metrology of large reflector antennas", *IEEE Trans. Antennas and Propagation*, **24**, 1976, p. 295.

[3] P. F. Scott and M. Ryle, "A rapid method for measuring the figure of a radio telescope reflector", *Mon. Notic. Roy. Astron. Soc.*, **178**, 1977, p. 539.

[4] Y. Rahmat–Samii, "Microwave holography of large reflector antennas–Simulation algorithms",*IEEE Trans. Antennas and Propagation*, **33**, 1985, pp. 1194-1203.

[5] D. Morris, J. W. M. Baars, H. Hein, H. Steppe, C. Thum and R. Wohleben, "Radio-holographic reflector measurement of the 30-m millimeter radio telescope at 22 GHz with a cosmic signal source", *Astron. Astrophys.*, **203**, 1988, pp. 399-406.

[6] M. P. Godwin, E. P. Schoessow and B. H. Grahl, "Improvement of the Effelsberg 100 meter telescope based on holographic reflector surface measurement", *Astron. Astrophys.*, **167**, 1986, p. 390.

[7] D. J. Rochblatt and B. L. Seidel, "Microwave antenna holography", *IEEE Trans. on Microwave Theory and Techniques*, **40**, 1992, pp. 1294-1300.

[8] J. W. M. Baars, R. N. Martin, J. G. Mangum, J. P. McMullin and W. L. Peters, "The Heinrich Hertz Telescope and the Submillimeter Telescope Observatory", *Publ. Astron. Soc. Pacific*, **111**, 1999, pp. 627-646.

[9] C. E. Mayer, J. H. Davis, W. L. Peters and W. J. Vogel, "A holographic surface measurement of the Texas 4.9m antenna at 86 GHz", *IEEE Trans. on Instruments and Measurements*, **IM-32**, 1983, 102-109.

[10] D. Morris, H. Hein, H. Steppe and J. W. M. Baars, "Phase retrieval radio holography in the Fresnel region - Tests on the 30 M telescope at 86 GHz", *IEE Proc. Part H*, **135**, 1988, pp. 61-64.

[11] R. Hills et al, "High-resolution millimetre-wave holography on the James Clerk Maxwell Telescope", URSI Assembly Maastricht, 2002

[12] H. Ezawa, M. Ishiguro, H. Matsuo, K. Miyawaki, N. Satou, and N. Ukita, *Proceedings of SPIE*, **4015**, 2000, p. 515.

[13] J. G. Mangum, J. W. M. Baars, A. Greve, R. Lucas, R. C. Snel, P. Wallace and M. Holdaway, "Evaluation of the ALMA prototype antennas", *Publ. Astron. Soc. Pacific*, **118**, 2006, pp. 1257-1301.

[14] S. Silver, "Microwave Antenna Theory and Design", *MIT Rad. Lab Series*, **12**, New York, McGraw-Hill, 1949.

[15] W. V. T. Rusch and P. D. Potter, "Analysis of Reflector Antennas", New York, Academic Press, 1970.

[16] R. Jennison, "Introduxtion to Radio Astronomy", London, Newnes, 1966.

[17] M. Born and E. Wolf, "Principles of Optics", Oxford, Pergamon Press, 1970, p.370.

[18] B. Lazareff, M. Carter, S. Halleguen and L. Degoud, "Characterization of holography horns for ALMA prototype antennas", IRAM internal report, 2003.

[19] R. Lucas and B. Glendenning, "ALMA test interferometer raw data format", ALMA Software Memo # 15, 2001

[20] L. R. D'Addario, "Holographic Antenna Measurements: Further Technical Considerations", NRAO 12-m Telescope Memo 202, 1982.

Jacob W. M. Baars received the M.Sc. and D.Sc. degrees in applied physics from the Technical University of Delft, the Netherlands in 1963 and 1970, respectively.

After working at the National Radio Astronomy Observatory in Green Bank, WV, he joined the Netherlands Foundation for Radio Astronomy in 1969. There he participated in the construction and was later head of the Westerbork Synthesis Radio Telescope. In 1975 he joined the Max-Planck-Institut für Radioastronomie in Bonn as head of the Division for Millimeter Technology. He was project Manager of the 30-m Millimeter Radio Telescope of IRAM in Spain and the Heinrich Hertz Telescope in Arizona. From 1997-99 he worked on the UMass-Mexico Large Millimeter Telescope. In 1999 he joined the European Southern Observatory, where he was involved in several aspects of the ALMA Project, lastly the evaluation of the prototype antennas. Since his retirement he consults in the area of large antennas and radio telescopes. His research interests are in the area of antenna theory and practice, in particular the performance calibration of large antennas with radio sources, and of atmospheric influences on observations at very high frequencies.

Max-Planck-Institut für Radioastronomie, Auf dem Hügel 69, D-53121 Bonn, Germany and European Southern Observatory, D-85748 Garching, Germany (jacobbaars@arcor.de)

Robert Lucas Robert Lucas received a Doctorat d'Etat from Paris University in 1976. After working with the Meudon Observatory and the Ecole Normale Supérieure in Paris, he joined the staff of the Grenoble University then the Institut de RadioAstronomie Millmétrique (IRAM) in Grenoble in 1987. He was closely associated with the commissioning of IRAM telescopes. He is now in charge of science software requirements for the ALMA project. His research interests include: line formation processes and chemistry in molecular clouds and circumstellar envelopes of evolved stars, the characterization of reflector antennas, the calibration of millimeter-wave interferometric data, and software for radioastronomy observations.

Institut de Radio Astronomie Millimétrique, 300 rue de la Piscine, Domaine Universitaire, 38406 Saint Martin d'Héres, France (lucas@iram.fr)

Jeffrey G. Mangum received the Ph.D. degree in astronomy from the University of Virginia in 1990.

Following a two-year residency as a postdoctoral researcher in the astronomy department at the University of Texas he joined the staff of the Submillimeter Telescope Observatory (SMTO) at the University of Arizona. In 1995 he joined the scientific staff at the National Radio Astronomy Observatory (NRAO) in Tucson, Arizona, and subsequently moved to the NRAO headquarters in Charlottesville, Virginia. His research interests include the astrophysics of star formation, the solar system, and external galaxies, the performance characterization of reflector antennas, and calibration of millimeter-wavelength astronomical measurements.

National Radio Astronomy Observatory, 520 Edgemont Road, Charlottesville, VA 22903, USA (jmangum@nrao.edu)

J. A. Lopez-Perez was born in Martos (Jaen), Spain, in 1971. He received the Telecommunication Engineer degree from the Universidad Politecnica de Madrid (UPM) in 1996.

Following a short period of time working at the Radiation Department of the UPM, he joined the Institut de Radio Astronomie Millimetrique (IRAM) in Grenoble (France) for two years. There he worked in the field of microwave antenna holography with David Morris and participated actively in the IRAM 30 meter radiotelescope holography campaigns during 1998, 1999 and 2000. In addition, he worked in the Backend Group of IRAM in the design and construction of electronic circuits for the Plateau de Bure Interferometer correlator.

After that, he joined the staff of the Observatorio Astronomico Nacional (OAN) in Yebes (Spain). There he was involved in the construction of the OAN 40 meter radiotelescope. He was also responsible for the design and construction of the 40-m holography receiver system and he led the construction of the digital autocorrelator spectrometer based in IRAM correlator boards.

In 2002, he worked in a feasibility study of a holography measurement system for the European Space Agency (ESA) ground antennas.

In 2003, he joined the ALMA Antenna Evaluation Working Group (AEWG) and worked in the holographic surface evaluation of the ALMA antenna prototypes in Socorro (NM,USA).

He is currently collaborating with INDRA company and the European Space Operation Center (ESOC) in the development of a holography system for the ESA Deep Space Antenna (DSA) system. He is also leading the construction of the 40-m X-band receiver for Very Long Baseline Interferometry (VLBI).

His main research interests are microwave holography of large reflector antennas and radioastronomy receiver design and development.

Centro Astronomico de Yebes, Apartado 148, E-19080 Guadalajara, Spain (ja.lperez@oan.es).